Yonghao Zhao[a], Ying Li[a], Troy D. Topping[a], Xiaozhou Liao[b], Yuntian Zhu[c], Ruslan Z. Valiev[d], Enrique J. Lavernia[a]

[a] Department of Chemical Engineering and Materials Science, University of California at Davis, Davis, CA, U.S.A.
[b] School of Aerospace, Mechanical & Mechatronic Engineering, The University of Sydney, Sydney, NSW, Australia
[c] Department of Materials Science and Engineering, North Carolina State University Raleigh, NC, U.S.A.
[d] Institute of Physics of Advanced Materials, Ufa State Aviation Technical University, Ufa, Russia

Ductility of ultrafine-grained copper processed by equal-channel angular pressing

In a previous study (R.Z. Valiev et al.: J. Mater. Res. 17 (2002) 5), unusual combinations of yield strength and ductility in ultrafine grained copper processed by equal-channel angular pressing of 360 MPa × 23 % (by Bc route two passes) and 380 MPa × 55 % (by Bc route 16 passes) were reported. However, results from recent work suggest that the tensile strain, when measured using a non-standard method and miniature dog-bone tensile specimens, is likely to contain significant errors. In this study, by implementing a standard strain measurement and tensile specimens with geometries that meet the ASTM requirements, we report yield strength and ductility combinations of 370 MPa × 9 % (Bc 2 passes) and 370 MPa × 16 % (Bc 16 passes) in the ultrafine grained copper. The higher ductility of the ultrafine grained copper processed by route Bc 16 passes was rationalized on the basis of several factors including the presence of equiaxed grains, lower dislocation density and higher fraction of high-angle grain boundaries (which result in larger strain rate sensitivity and strain hardening).

Keywords: Ultrafine grained copper; Standard mechanical testing; Ductility; Microstructure

1. Introduction

Since 1981, bulk nanostructured (ns) materials have emerged as a new class of materials and have attracted attention as potential candidates for next-generation structural materials applications [1, 2]. Indeed, success has been achieved on the strength improvement with grain size refinement to nano-scale, extrapolated from the well-known Hall–Petch relation (at least down to ∼ 20 nm) [3]. However, numerous studies published before 2000 indicated that bulk ns materials usually have relatively low strain to failure (ductility) at ambient temperatures [3–6], which has remained as a seemingly insurmountable obstacle in many practical applications.

Recent investigations on developing strategies [7, 8] to improve the poor ductility of ns materials relate to two landmark papers, which appeared in 2002 [9, 10]. The importance of these two papers is attested by the large number of citations: 329+ and 487+, respectively. In Ref. [9], attractive combinations of yield strength and ductility in ultrafine grained (UFG) Cu by equal-channel angular pressing (ECAP) of 360 MPa × 23 % (by route Bc 2 passes) and

380 MPa × 55 % (by Bc 16 passes) were reported. However, in this particular study the tensile strain was measured based on crosshead displacement and using miniature dog-bone tensile specimens with a gauge length of 5 mm, and cross-section of 1 × 2 mm. In this case the ratio of gauge length to width is 2.5. Based on ASTM standards [11], a subsize rectangular tensile specimen should have a gauge length of 25 mm, a width of 6 mm and a thickness less than 6 mm. Hence, the ratio of gauge length to width should be maintained at a value of approximately 4 in order to comply with ASTM standards. More recently, by using both experiments and finite element modeling (FEM) [12, 13], we reported that in the absence of accurate strain measurement techniques, such as those based on digital image correlation or laser interferometry, strains derived based on cross-head displacement may contain non-negligible errors and are particularly sensitive to specimen geometry: both uniform elongation (strain before onset of necking) and post-necking elongation increase with decreasing gauge length and increasing specimen thickness/width [13]. The experimental error derived from the measurement of strain on the basis of crosshead displacement was attributed to the contributions of machine compliance of the loading frame and gauge corner deformation which increases with increasing thickness/width and decreasing gauge length [13]. Therefore, it is now necessary to re-evaluate the mechanical properties of the UFG Cu by using standardized mechanical testing and tensile specimens with geometries that are consistent with ASTM requirements.

In this work, we measured the strain of the UFG Cu processed by ECAP route Bc [14] by using a standard non-contacting video extensometer with a 100 mm field of view lens and tensile specimens with gauge dimensions of 10 × 1 × 2 mm. We achieved yield strength and ductility combinations of 370 MPa × 9 % (for UFG Cu by ECAP Bc 2 passes) and 370 MPa × 16 % (UFG Cu by ECAP Bc 16 passes). The difference in ductility between the UFG Cu processed by ECAP Bc routes 2 and 16 passes was rationalized on the basis of microstructure-based deformation mechanisms.

2. Experiments

The experimental procedure is described as follows. High-purity copper (99.99 %) square bars (20 × 20 mm) were processed by ECAP at ambient temperature by route Bc

for 2 and 16 passes, respectively (henceforth designated as the samples ECAP-2 and ECAP-16). The ECAP die has an intersecting channel angle of 90° and an outerarc angle of 45°.

Flat dog-bone tensile specimens with gauge dimensions of $10 \times 1 \times 2$ mm were sectioned by electrical discharge machining (EDM) from the central regions of the UFG Cu square bars with a gauge axis parallel to the extrusion direction and a gauge surface parallel to top plane of the extrusion bar. All tensile specimens were finally polished using a diamond suspension with particle size of 0.25 μm. Three samples were prepared for each condition in order to ensure reproducibility of results. Uniaxial tensile tests were performed at room temperature on an Instron 8801 universal testing machine (UTM) using Bluehill 2 software with an initial quasi-static strain rate of 10^{-3} s^{-1}. The strain was measured by using a standard non-contacting video extensometer with a 100 mm field-of-view lens. Jump tests were performed using three different strain rates: $2 \cdot 10^{-5}$ s^{-1}, $5 \cdot 10^{-4}$ s^{-1} and $1 \cdot 10^{-2}$ s^{-1}, and the strains to jump were 0.8 and 1.6%, respectively.

The grip sections of the tensile specimens were examined using transmission electron microscopy (TEM). TEM specimens were prepared by first mechanically grinding the samples to a thickness of about 20–30 μm, then dimpling to a thickness of about 10 μm, and finally ion-milling to a thickness of electron transparency using a Gatan Precision Ion Milling System with an Ar+ accelerating voltage of 4 kV and a temperature below 35 °C. TEM observations were conducted with a Philips CM12 microscope operated at 100 kV. Quantitative X-ray diffraction (XRD) measurements were performed on a Scintag X-ray diffractometer equipped with a Cu target operating at 1.8 kW. $\theta-2\theta$ scans were performed to record the XRD patterns at room temperature. Pure Cu powder (99.99%) was annealed at 200 °C in Ar and used as an XRD peak-broadening reference for the grain size and microstrain calculations [15, 16]. The peak parameters (peak intensity, peak-maximum position, full width at half maximum and integral breadth) were determined by fitting a Pearson VII function to the measured peaks. The fracture surface was imaged by an FEI-XL30 SFEG scanning electron microscopy using a 25 kV beam.

3. Results

The representative engineering stress–strain curves of the UFG Cu samples are compared in Fig. 1. It is apparent that both samples exhibit 0.2% yield strengths of 370 MPa (as marked by an open circle) and dominant post-necking elongations in the stress–strain curves, which is typical of UFG metals processed by severe plastic deformation because of the low dislocation storage capacity. In more detail, the ECAP-16 sample has a slightly larger uniform elongation (2%, designated by a black arrow) and ultimate tensile strength (400 MPa) compared with those of the ECAP-2 sample (1% and 370 MPa, designated by a gray arrow). After the onset of necking, the reduction in the stress against strain (strain-hardening rate) in the sample ECAP-16 was much slower than that in sample ECAP-2, giving rise to a larger elongation to failure of 16% compared with 9% for ECAP-2. The error associated with these ductility values is less than 1%. The higher ductility and ultimate
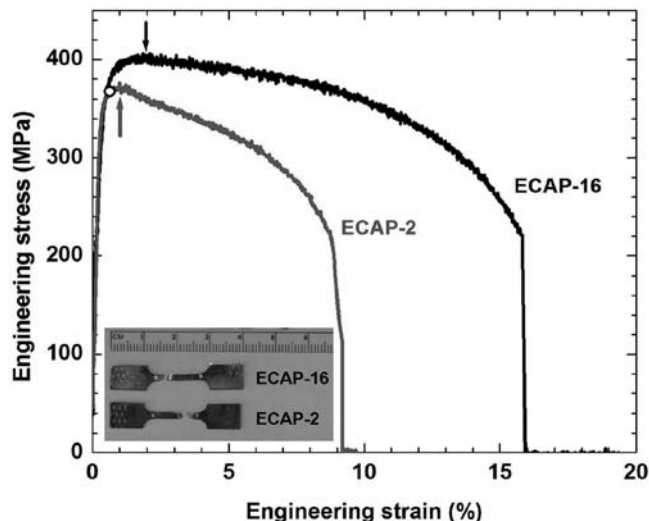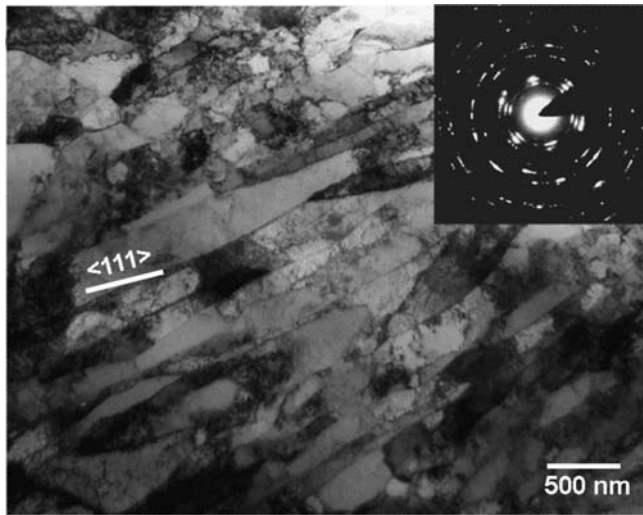

Fig. 1. Tensile engineering stress–strain curves of the UFG Cu samples ECAP-2 and ECAP-16 at a strain rate of 10^{-3} s^{-1}. The inset shows fractured tensile specimens with gauge dimensions of $10 \times 2 \times 1$ mm. The yield strength is marked by an open circle, and the ultimate tensile strengths of the ECAP-16 and ECAP-2 are indicated by black and gray arrows, respectively. The open circles are overlapped since the UFG Cu samples of ECAP-2 and ECAP-16 have the same yield strength.

tensile strength values of ECAP-16, as compared to those of ECAP-2 is consistent with previous work [9]. However, the absolute values of uniform elongation and ductility are much smaller than those reported in Ref. [9], which are 4 (ECAP-2) and 8% (ECAP-16), and 23 (ECAP-2) and 55% (ECAP-16), respectively, as compared in Table 1. As discussed in the introduction part, the differences in uniform elongation and ductility between the present work and Ref. [9] are caused by different tensile specimen sizes and strain measurement methods. In addition, enhanced ductility of ECAP-Cu with increasing ECAP passes was also reported elsewhere [17].
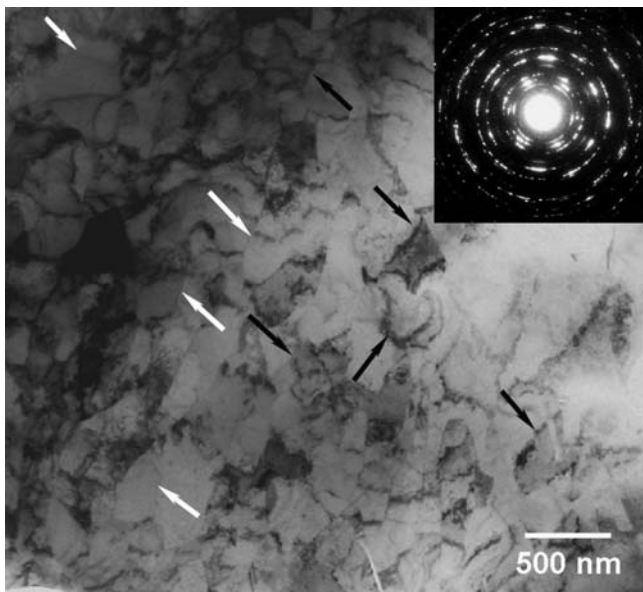
Figure 2 presents typical bright-field TEM images and the corresponding selected area diffraction (SAD) patterns (taken from an area with a diameter of 5.4 μm) of the samples ECAP-2 (viewed close to a <110> zone axis) and ECAP-16. The sample ECAP-2 was mainly composed of parallel lamellar boundaries (LB) with strongly elongated subgrains and an average width of about 350 nm and a length of ~1000 nm. The LBs are approximately parallel to the tensile axis. In Ref. [18], LB is similar to dense dislocation walls enclose several cells and are classified as geometrically necessary boundaries, since they are necessary

Table 1. Comparison of yield strength $\sigma_{0.2}$, ultimate tensile strength σ_{UTS}, uniform elongation ε_{ue} and elongation to failure ε_{ef} of the ECAP-16 and ECAP-2 samples in present study with previous work [9].

	Samples	$\sigma_{0.2}$ (Mpa)	σ_{UTS} (Mpa)	ε_{ue} (%)	ε_{ef} (%)
Previous [9]	ECAP-16	380	440	8	55
	ECAP-2	360	390	4	23
Present work	ECAP-16	370	400	2	16
	ECAP-2	370	370	1	9

Y. Zhao et al.: Ductility of ultrafine-grained copper processed by equal-channel angular pressing

(a)

(b)

Fig. 2. Bright-field TEM images and the corresponding selected area diffraction (SAD) patterns (taken from an area with a diameter of 5.4 μm) of samples (a) ECAP-2 viewed close to <110> zone axis and (b) ECAP-16. Sharp and straight equilibrium boundaries and wavy distorted subgrain (dislocation cell) boundaries are pointed by white and black arrows in Fig. 2b, respectively. The innermost ring in SAD patterns might originate from CuO due to oxidation.

to accommodate the glide-induced lattice rotation in the adjoining volume. The LBs are mainly low-angled, as verified by the clustered diffraction spots in the SAD patterns, and aligned mainly along trace of a {111} plane. Dislocation cell boundaries are present inside the LBs. In contrast, sample ECAP-16 is composed of equiaxed grains with an average size of about 300 nm. In literature, smaller average grain sizes were reported in UFG Cu by ECAP Bc route as 100 nm for ECAP-16 and 200 nm in ECAP-15 [17]. These differences in average grain size might be caused by different measurement planes relative to the extrusion direction and/or calculation error. The ring-like SAD pattern shows that the grain boundaries are mainly of a high-angle type. Moreover, two types of boundaries were observed: sharp

and straight equilibrium boundaries (as indicated by white arrows) and wavy distorted boundaries (indicated by black arrows in the figure). The sharp equilibrium boundaries may have originated from relaxation and recovery during the ECAP process, and these represent approximately 20 % of the overall boundaries. The wavy distorted boundaries are mainly subgrain (dislocation cell) boundaries with low-angle misorientation. Part of the wavy distorted boundaries might be non-equilibrium boundaries. From literature, the non-equilibrium boundaries contain a high density of extrinsic dislocations, which are not needed to accommodate the misorientation across the grain boundary [19]. The above microstructural characteristics during the ECAP process are consistent with the results reported in the literature [9, 17, 20, 21].

The dislocation density, measured by the XRD peak broadening method [15, 16], is $2 \cdot 10^{14}$ m^{-2} for ECAP-2 and $1 \cdot 10^{14}$ m^{-2} for ECAP-16. Extensive deformation lowering the dislocation density has frequently been reported [16, 22, 23]. When dislocation density was saturated, further deformation activated dislocation recovery and evolution to grain boundaries. As shown in Fig. 3, strong (111) peaks indicate that both samples have (111) texture.

To understand the larger post-necking elongation in the ECAP-16 as compared to that in the ECAP-2, we studied the fracture mode and morphology using the SEM. Figure 4 shows SEM images of the fracture surfaces of samples ECAP-2 and ECAP-16. The fracture area reduction of the ECAP-2 is 69 %, slightly smaller than that of the ECAP-16 (73 %). From Fig. 4b and d, however, the samples have similar dimple sizes ranging from about 5 to 20 μm. The dimples in the ECAP-16 are slightly elongated due to void nucleation and subsequent coalescence via shear fracture, as verified below.

Figure 5 shows the SEM cross-sectional images of both ECAP-2 and ECAP-16 samples. Sample ECAP-2 failed in a normal tensile fracture mode with a shear fracture angle of about 90° (Fig. 5a). The shear fracture angle is defined as the angle between the load direction and the fracture surface. Sample ECAP-16 failed in a shear fracture mode with a shear fracture angle of about 70° (Fig. 5c). The shear fracture is attributable to the nanostructures which resulted in a
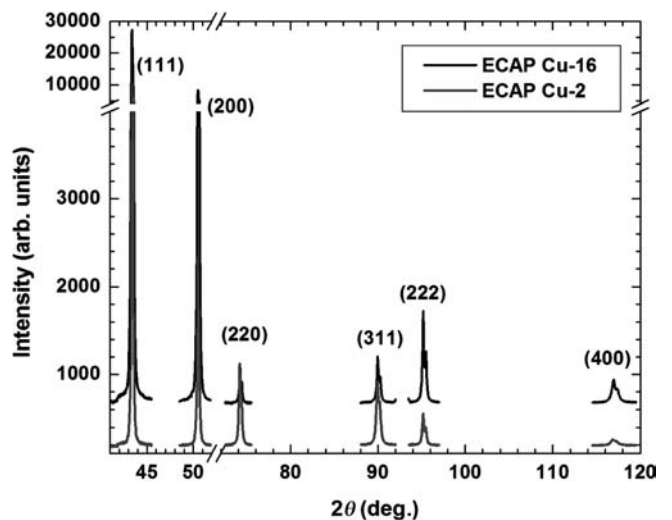

Fig. 3. XRD patterns of samples ECAP-2 and ECAP-16. Both samples have (111) texture.
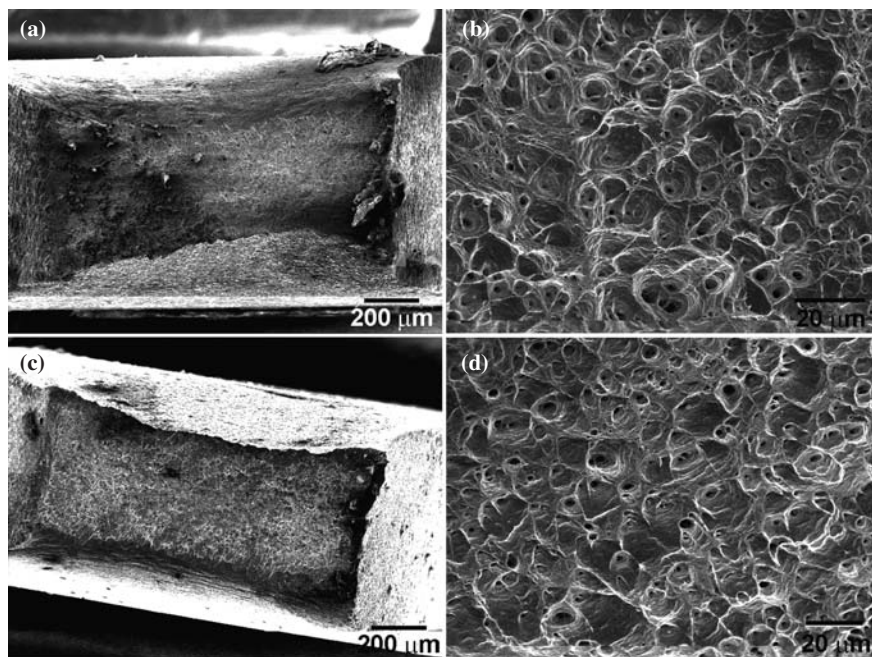
Fig. 4. SEM images of the fracture surfaces of samples (a, b) ECAP-2 and (c, d) ECAP-16. The fracture area reduction of the ECAP-2 is 69 %, slightly smaller than that of the ECAP-16 (73 %). The samples have similar dimple sizes ranging from about 5 to 20 μm. The dimples in the ECAP-16 are slightly elongated due to void nucleation and subsequent coalescence via shear fracture.
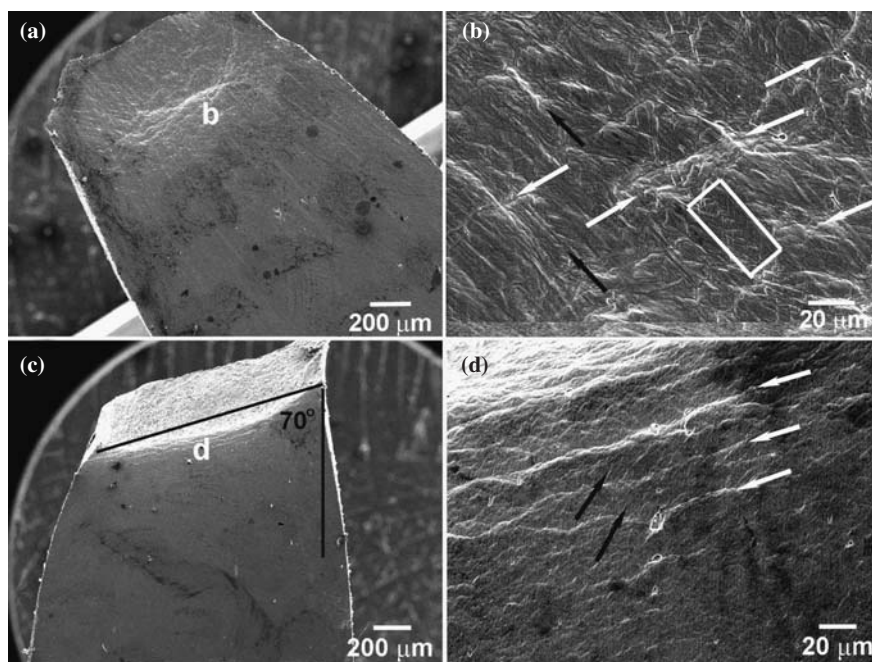

Fig. 5. Cross-sectional SEM images showing fracture morphologies of samples (a, b) ECAP-2 and (c, d) ECAP-16. Sample (a) ECAP-2 failed in a normal fracture mode and (c) ECAP-16 failed in a shear fracture mode. (b) (d) are magnified images of the regions marked by "b" and "d" in Fig. (a) and (c), respectively. Deformation bands are marked by white and black arrows in (b) and (d). Slip bands was marked by rectangle in (b).

decreased ratio of the average critical normal fracture stress to shear fracture stress [24]. Careful examination on the cross-sectional surface near the fracture edge revealed some coarse steps/networks parallel to fracture edge with a distance of tens of micrometers (denoted by white arrows in Fig. 5d), and fine steps/networks with a distance of several micrometers between the coarse steps (denoted by black arrows in Fig. 5d) in sample ECAP-16. The coarse steps become much more discontinuous in sample ECAP-2, as denoted by white arrows in Fig. 5b. Moreover, many "striations" were evident parallel to the tensile axis (as denoted by black arrows in Fig. 5c) in which slip bands with an orientation of about 45° to the tensile axis and a width in the micrometer range were found (as marked by a rectangle in Fig. 5c). This surface morphology may have evolved

from the elongated subgrain structures. The above results suggest that the equiaxed grains in sample ECAP-16 are favorable to form finer micro-deformation steps, resulting in the larger post-necking elongation.

To further explain the larger ductility of ECAP-16, as compared with ECAP-2, we completed a series of strain jump tests. Figure 6 shows the true stress–strain curves of ECAP-2 and ECAP-16 in jump tests using three different strain rates: $2 \cdot 10^{-5}$ s^{-1}, $5 \cdot 10^{-4}$ s^{-1} and $1 \cdot 10^{-2}$ s^{-1}. The strain rate sensitivity value m is defined via a power law relation [25]:

$$\sigma/\sigma_0 = (\acute{\varepsilon}/\acute{\varepsilon}_0)^m \qquad (1)$$

where σ and $\acute{\varepsilon}$ are true stress and strain rate. The calculated average m value was 0.014 for ECAP-16 and 0.010 for

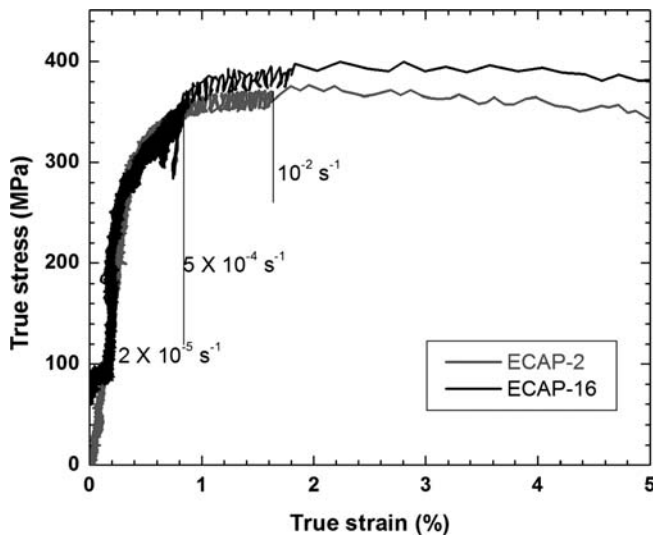Y. Zhao et al.: Ductility of ultrafine-grained copper processed by equal-channel angular pressing

Fig. 6. True stress–strain curves of ECAP-2 and ECAP-16 in jump tests. Three strain rates were used: $2 \cdot 10^{-5}$ s^{-1}, $5 \cdot 10^{-4}$ s^{-1} and $1 \cdot 10^{-2}$ s^{-1}.

ECAP-2. According to the Hart criterion [26], a large m value is expected to delay the onset of necking for a rate-sensitive material. However, we note that the strain rate sensitivity increase in the ECAP-16 sample is only 0.04, which does not much change the uniform elongation (or necking point). The higher strain rate sensitivity is also expected to enhance the post necking strain, although it is not clear how much enhancement will be produced.

4. Discussion

For ns metals, a convincing theory that can be used to explain strain hardening behavior has not been formulated. It has been reported that the ns fcc metals typically involve high strain rate sensitivity values [6, 8, 27–30]. According to Hart's classical analysis [26], the strain rate sensitivity should make a contribution to whatever amount of ductility is present in ns metals.

According to Hart's analysis, assuming the initial uniform cross-section of the specimen is A_0, a small segment of the specimen has a cross-section deviating from this uniform value by δA_0. After a certain time interval δt, A_0 has changed to A with the special segment evolved into $(A + \delta A)$. Then the evolution of dA reflects the growth of inhomogeneities (or necking instabilities) within the specimen [26], which depends on the strain rate sensitivity as:

$$\delta A = (A_0/A)^{1/m-1}(\delta A_0) \qquad (2)$$

Equation (2) was derived by Hart assuming the strain hardening vanishes. It indicates that the growth of inhomogeneities of a tensile specimen with negligible strain hardening strongly depends on the strain rate sensitivity of the material being tested. An increase in the value of m will retard the growth of inhomogeneities as has been observed for many ns fcc metals [6, 8, 9, 27–30]. In fact, in 1981, Lin and coworkers had observed that metals and alloys with vanishing strain hardening but with strain rate sensitivity with values ~0.02 can readily attain fracture elongation values of 10 % [31]. This observation suggests the importance of

strain rate sensitivity in suppressing the growth of plastic instabilities.

Except for the enhanced m value, the greater ductility of ECAP-16 might also be attributed to its higher strain hardening exponent, which may be rationalized on the basis of a low dislocation density, and the presence of equi-axed grains and high fraction of high-angle grain boundaries. The strain hardening that is evident in the uniform deformation of sample ECAP-16 originated from a small amount of large grains with low dislocation density, which still possesses the ability to accumulate dislocations. The low dislocation density in ECAP-16 can result in an enhancement in strain hardening and decrease in dynamic recovery rate, and therefore, a larger post-necking elongation. Moreover, it has been reported that high-angle grain boundaries are beneficial to high ductility [32, 33]. However, from the current results, the contributions to enhanced ductility from increases in strain rate sensitivity and strain hardening could not be quantitatively separated.

The unchanged yield strength in samples ECAP-2 and ECAP-16 can be explained as follows: 16 ECAP passes decrease dislocation density which in turn is anticipated to decrease the yield strength. However, the above loss in yield strength might be compensated by grain refinement strengthening, resulting in the same yield strength.

5. Conclusions

In summary, we provide a report on accurate tensile mechanical properties for UFG Cu processed by ECAP 2 and 16 passes by using standardized mechanical testing and tensile specimens with geometries that comply with ASTM requirements: yield strength and ductility combinations of 370 MPa × 9 % (for UFG Cu by 2 passes) and 370 MPa × 16 % (UFG Cu by 16 passes). Compared with the UFG Cu by 2 passes, the higher ductility of the UFG Cu by 16 passes was rationalized on the basis of its equiaxed grains, lower dislocation density, higher fraction of high-angle grain boundaries which result in larger strain rate sensitivity and strain hardening.

References

[1] H. Gleiter, in: N. Hansen, A. Horsewell, T. Leffers, H. Lilholt (Eds.), Proceedings of the second Risφ International Symposium on Metallurgy and Materials Science, Risφ National Laboratory Roskilde, Denmark (1981) 5.
[2] M.A. Meyers, A. Mishra, D.J. Benson: Prog. Mater. Sci. 51 (2006) 427. DOI:10.1016/j.pmatsci.2005.08.003
[3] J.R. Weertman, in: C.C. Koch (Ed.), Nanostructured Materials: Processing, Properties and Applications, 2nd Ed., William Andrews Publishing, Norwich, New York (2007) 537.
[4] C.C. Koch, D.G. Morris, K. Lu, A. Inoue: MRS Bull. 24 (1999) 54.
[5] C.C. Koch: Scripta Mater. 49 (2003) 657. DOI:10.1016/S1359-6462(03)00394-4
[6] E. Ma: Scripta Mater. 49 (2003) 663. DOI:10.1016/S1359-6462(03)00396-8
[7] C.C. Koch, K.M. Youssef, R.O. Scattergood, K.L. Murty: Adv. Eng. Mater. 7 (2005) 787, references therein. DOI:10.1002/adem.200500094
[8] E. Ma: JOM 58(4) (2006) 49, references therein. DOI:10.1007/s11837-006-0215-5
[9] R.Z. Valiev, I.V. Alexandrov, Y.T. Zhu, T.C. Lowe: J. Mater. Res. 17 (2002) 5. DOI:10.1557/JMR.2002.0002

[10] Y.M. Wang, M.W. Chen, F.H. Zhou, E. Ma: Nature 419 (2002) 912. PMid:12410306; DOI:10.1038/nature01133

[11] ASTM E 8M-04: http://www.astm.org

[12] Y.H. Zhao, Y.Z. Guo, Q. Wei, A.M. Dangelewicz, C. Xu, Y.T. Zhu, T.G. Langdon, Y.Z. Zhou and E.J. Lavernia: Scripta Mater. 59 (2008) 627. DOI:10.1016/j.scriptamat.2008.05.031

[13] Y.H. Zhao, Y.Z. Guo, Q. Wei, T.D. Topping, A.M. Dangelewicz, Y.T. Zhu, T.G. Langdon, E.J. Lavernia: Mater. Sci. Eng. A 525 (2009) 68. DOI:10.1016/j.msea.2009.06.031

[14] Y. Iwahashi, Y. Wang, Z. Horita, M. Nemoto, T.G. Langdon: Scripta Mater. 35 (1996) 143. DOI:10.1016/1359-6462(96)00107-8

[15] L.H. Qian, S.C. Wang, Y.H. Zhao, K. Lu: Acta Mater. 50 (2002) 3425. DOI:10.1016/S1359-6454(02)00155-6

[16] Y.H. Zhao, K. Lu, K. Zhang: Phys. Rev. B 66 (2002) 085404. DOI:10.1103/PhysRevB.66.085404

[17] S.V. Dobatkin, J.A. Szpunar, A.P. Zhilyaev, J.-Y. Cho, A.A. Kuznetsov, Mater. Sci. Eng. A 462 (2007) 132. DOI:10.1016/j.msea.2006.04.156

[18] D.A. Hughes, N. Hansen: Acta Mater. 48 (2000) 2985. DOI:10.1016/S1359-6454(00)00082-3

[19] J.Y. Huang, Y.T. Zhu, H. Jiang, T.C. Lowe: Acta Mater. 49 (2001) 1497. DOI:10.1016/S1359-6454(01)00069-6

[20] R.Z. Valiev, R.K. Isamgaliev, I.V. Alexandrov: Prog. Mater. Sci. 45 (2000) 103. DOI:10.1016/S0079-6425(99)00007-9

[21] R.Z. Valiev, T.G. Langdon: Prog. Mater. Sci. 51 (2006) 881. DOI:10.1016/j.pmatsci.2006.02.003

[22] Y.H. Zhao, H.W. Sheng, K. Lu: Acta Mater. 49 (2001) 365. DOI:10.1016/S1359-6454(00)00310-4

[23] F. Dalla Torre, R. Lapovok, J. Sandlin, P.F. Thomson, C.H.J. Davies, E.V. Pereloma: Acta Mater. 52 (2004) 4819. DOI:10.1016/j.actamat.2004.06.040

[24] Z.F. Zhang, J. Eckert: Phys. Rev. Lett. 94 (2005) 094301. PMid:15783967; DOI:10.1103/PhysRevLett.94.094301

[25] M.A. Meyer, K.K. Chawla: Mechanical Metallurgy, Englewood Cliffs (NJ), Prentice-Hall (1984) 570 and 585.

[26] E.W. Hart: Acta Metall. 15 (1967) 351. DOI:10.1016/0001-6160(67)90211-8

[27] Y.M. Wang, E. Ma: Acta Mater. 52 (2004) 1699. DOI:10.1016/j.actamat.2003.12.022

[28] Q. Wei: J. Mater. Sci. 42 (2007) 1709. DOI:10.1007/s10853-006-0700-9

[29] Q. Wei, S. Cheng, K.T. Ramesh, E. Ma: Mater. Sci. Eng. A 381 (2004) 71. DOI:10.1016/j.msea.2004.03.064

[30] R.J. Asaro, S. Suresh: Acta Mater. 53 (2005) 3369. DOI:10.1016/j.actamat.2005.03.047

[31] I.H. Lin, J.P. Hirth, E.W. Hart: Acta Metall. Mater. 29 (1981) 819. DOI:10.1016/0001-6160(81)90124-3

[32] Y.H. Zhao, J.F. Bingert, X.Z. Liao, B.Z. Cui, K. Han, A. Serhueeva, A.K. Muhkerjee, R.Z. Valiev, T.G. Langdon, Y.T. Zhu: Adv. Mater. 18 (2006) 2949. DOI:10.1002/adma.200601472

[33] Y.H. Zhao, J.F. Bingert, Y.T. Zhu, X.Z. Liao, R.Z. Valiev, Z. Horita, T.G. Langdon, Y.Z. Zhou, E.J. Lavernia: Appl. Phys. Lett. 92 (2008) 081903. DOI:10.1063/1.2870014

Bibliography

Correspondence address

Yonghao Zhao, Ph.D.
Assistant Project Scientist
Dept. Chemical Engineering and Materials Science
University of California, Davis
1231 Bainer Hall, One Shields Avenue
Davis, CA 95616-5294
Tel./Fax: 530-752-9568/9554
E-mail: yhzhao@ucdavis.edu